JOURNAL OF GEOPHYSICAL RESEARCH, VOL. 112, E11002, doi:10.1029/2007JE002894, 2007

Modeling impact cratering in layered surfaces

Laurel E. Senft[1] and Sarah T. Stewart[1]

Received 12 January 2007; revised 15 June 2007; accepted 6 September 2007; published 7 November 2007.

[1] Impact craters are potentially powerful tools for probing large-scale structure beneath planetary surfaces. However, the details of how target structure affects the impact cratering process and final crater forms remain poorly understood. Here, we present a study of cratering in layered surfaces using numerical simulations. We implement the rheologic model for geologic materials described by Collins et al. (2004) into the shock physics code CTH; this model includes pressure, temperature, and damage effects on strength as well the option to include acoustic fluidization. The model produces reasonable final crater shapes and damaged zones from laboratory to planetary scales. We show the effects of varying material strength parameters and discuss choosing appropriate strength parameters for laboratory and planetary situations. Results for cratering into idealized terrains with layers of differing material strength are presented. The presence of such layers in the target can significantly alter the ejecta curtain structure and the final crater morphology. Finally, we reproduce the morphologic variations that are observed in small lunar craters by modeling a weak regolith overlying competent rock.

Citation: Senft, L. E., and S. T. Stewart (2007), Modeling impact cratering in layered surfaces, *J. Geophys. Res.*, *112*, E11002, doi:10.1029/2007JE002894.

1. Introduction

[2] Impact cratering is a major geologic process that has shaped the surfaces of almost all of the terrestrial planets and satellites. The final crater morphology produced by an impact event is determined by a number of properties, including gravity, the size and velocity of the impactor, and the material properties of both the target and the impactor. Because crater morphology is affected by material properties that are below the target surface, craters provide an ideal way to probe features that are hidden from view. In addition, because impact cratering is a process that has occurred ubiquitously throughout the solar system and throughout the solar system's history, surfaces of all ages on a planet can be studied using the same methods, allowing the construction of histories and maps of the subsurface.

[3] Layering is an abundant feature in our solar system, including on the Earth, Mars [*Beyer and McEwen*, 2005; *Edgett and Malin*, 2002; *Malin and Edgett*, 2000], the Moon [*Gault et al.*, 1966], the icy satellites [*Schenk*, 2002; *Showman and Malhotra*, 1999], and possibly comets [*Belton et al.*, 2007; *Belton and Deep Impact Science Team*, 2006]. During the last few decades, progress has been made toward understanding the effects that target layers have on the impact cratering process and final crater morphologies. Laboratory studies of impacts into layered targets have shown significant changes in crater and ejecta blanket morphologies [*Oberbeck and Quaide*, 1967; *Piekutowski*, 1977; *Quaide and Oberbeck*, 1968; *Schultz*, 1992]. Numerical studies of impacts into marine (layered water over competent rock) targets have displayed morphologic variations which are dependent upon the thickness of the water layer and the size of the impactor [*Lindstrom et al.*, 2005; *Ormö et al.*, 2002, 2004; *Shuvalov and Trubestkaya*, 2002]. Furthermore, numerical studies of impacts into marine targets including a weak sedimentary surface layer have been used to explain the morphology of the Chesapeake Bay impact structure in Virginia and the Mjolnir impact structure in the Barents Sea [*Collins and Wunnemann*, 2005; *Shuvalov et al.*, 2002]. Finally, *Head et al.* [2002] has used numerical simulations to show that the presence of a regolith reduces spall velocities (spall is believed to be the mechanism for meteorite ejection). However, much work remains to be done on the general problem of how solid layers in the target affect crater and ejecta blanket morphologies at the planetary scale.

[4] This paper presents an initial study of the topic. In section 2, we implement and validate the strength model for rocks described by *Collins et al.* [2004] into the shock physics code CTH (sections 2.1 and 2.2) and discuss appropriate choices for model input parameters (section 2.3). In sections 3.1 and 3.2, we use numerical simulations to illustrate the observable effects resulting from target layering. As an example of how crater forms can be used to probe subsurface layering, we demonstrate that the morphologic variations of small lunar craters can be reproduced by modeling a regolith overlying competent rock (section 3.3).

2. Strength Model

[5] Craters produced in the laboratory are limited in scale; thus to simulate the large-scale cratering events that are

[1]Department of Earth and Planetary Sciences, Harvard University, Cambridge, Massachusetts, USA.

0148-0227/07/2007JE002894$09.00

Table 1. Input Parameters for Strength Model

Variable	Definition
Y_o	shear strength of intact rock at zero pressure
Y_m	limiting (Von Mises) shear strength as pressure increases
μ_i	coefficient of internal friction of intact rock
μ_d	coefficient of internal friction of damaged (fragmented) rock
T_m	melting temperature
ξ	thermal softening parameter
Y_{to}	maximum tensile strength
P_{bd}	brittle to ductile transition pressure
P_{bp}	brittle to plastic transition pressure
G	shear modulus at ambient pressure and temperature
K_o	bulk modulus at ambient pressure and temperature
Y_c	cohesion at zero pressure
D_{so}	initial shear damage
D_{to}	initial tensile damage
η	acoustic fluidization viscosity
t_{off}	time to turn off new acoustic fluidization pressure vibrations
C_{vib}	maximum vibration particle velocity (fraction of the maximum velocity)
τ	acoustic fluidization decay constant

common in our solar system, we must use numerical experiments. This is typically done through the use of shock physics codes, which are codes that track the stresses and strains through time of large-scale deformation events. Shock physics codes work by simultaneously solving three components: (1) the equations for the conservation of mass, momentum, and energy, (2) an equation of state (EOS), which describes the response of a material to volumetric stresses, and (3) a constitutive (or strength) model, which describes the response of a material to deviatoric stresses. The equation of state and the constitutive model are material dependent. The validity of the results produced by any given numerical experiment is highly dependent upon the quality of the EOS and constitutive model used.

[6] We use the shock physics code CTH [*McGlaun et al.*, 1990]. CTH employs an Eulerian mesh with a Lagrangian step in time. During the Lagrangian step, finite volume approximations of the conservation equations, equation of state, and constitutive model equations are solved, advancing the stress, strain, velocities, and so on in time. This is followed by a remap step, which maps the deformed mesh back to the original Eulerian mesh. Additionally, massless Lagrangian tracers can be embedded into materials to track the history of a mass element through time. The capabilities of CTH include the ability to handle complicated equations of state involving heating and phase changes, as well as multimaterial cell thermodynamics, meaning that multiple materials can occupy a computational cell with each material having its own temperature and pressure. A major advantage of CTH is its utilization of adaptive mesh refinement (AMR), which increases or decreases the density of the Eulerian mesh with time and location according to user specified indicators [*Crawford*, 1999]. This allows the shock front and finely spaced layers at the surface to be resolved without expending too much computational energy elsewhere in the problem domain. However, existing strength models in CTH to describe the behavior of geological materials (rocks) are very simple and more sophisticated models, developed for ceramics, have numerous parameters that are difficult to obtain. Thus we implement into CTH an improved empirical strength model for rocks, which is based upon bulk material properties, to more accurately describe impacts into such targets.

2.1. Model Description

[7] We implement the strength model described in *Collins et al.* [2004]; precursor work to their model was conducted by *Ivanov et al.* [1997]. For a detailed description, refer to these papers and to Appendix A of this paper. Briefly, rocks fail in shear or tension. A rock behaves elastically up to some shear/tensile stress known as the shear/tensile strength; once this strength is exceeded, the shear/tensile stress can no longer increase with increasing strain. Both the shear and tensile strength depend upon a number of factors, for example, pressure, temperature, strain rate, fracturing, porosity, and fluid pressure. The model calculates shear strength as a function of pressure, temperature, and total damage. Damage is a dimensionless quantity which describes the density of fracturing that a material has experienced; damage ranges from zero (for completely intact material) to one (for completely fragmented material). Tensile strength is calculated as a function of temperature and total damage. Shear and tensile damage are tracked separately; shear damage is accumulated with integrated plastic strain, while tensile damage is accumulated according to a simple crack growth model. Under tensile failure, void space is added to a computational cell to simulate fracture until the maximum (most tensile) principal stress in the cell equals the limiting tensile strength.

[8] The formulation described so far will accurately describe the formation of simple craters; however, the formation of complex craters requires an additional weakening mechanism that operates during crater collapse to reach the final crater diameter and reproduce observed structural deformation. While it is unclear exactly what this mechanism is, the most widely tested model to date is the block model approximation of acoustic fluidization [*Collins*, 2002; *Collins et al.*, 2004; *Ivanov and Kostuchenko*, 1997; *Melosh and Ivanov*, 1999; *Wunnemann and Ivanov*, 2003]. In this model, impacts induce pressure vibrations in the target. These vibrations, which dampen with time, temporarily reduce the overburden pressure and allow the material to flow. The model includes acoustic fluidization as an option in the calculation.

[9] The strength model requires eighteen input parameters (fourteen for the strength-damage part, four for acoustic fluidization); these parameters are defined in Table 1. The strength-damage model parameters represent fundamental material properties, while the acoustic fluidization parameters are empirically fitted to match lunar, terrestrial, and Venusian craters [*Collins*, 2002; *Wunnemann and Ivanov*, 2003]. In CTH, this model has been named the ROCK model to distinguish it from other available strength models.

2.2. Model Validation

[10] We tested the strength model in order to validate its accuracy. These include comparisons to (1) other numerical studies, (2) laboratory experiments, (3) crater scaling laws, and (4) terrestrial field observations. All simulations shown in this paper are two-dimensional cylindrically symmetric calculations.

Table 2. Strength Parameters Used in Simulations Presented in Figures[a]

	Figures 1 and 5 (Squares)	Figures 2–4	Figure 5 (Circles)	Figures 7a, 8a, and 9 ("Strong")	Figures 7b and 8b	Figures 7c, 8c, and 9 ("Normal") and 12 and 13 (Competent Rock)	Figure 9 ("Weak")	Figure 10 ("Normal")	Figure 10 ("Weak")	Figure 10 ("Strong")	Figure 12 (Regolith)	Figure 13 (Regolith)
Y_o	90 MPa	900 MPa	0.9 MPa	10 MPa	1 MPa	0.1 MPa	0.001 MPa	0.1 MPa	0.001 MPa	10 MPa	0.1 MPa	0.1 MPa
Y_m	1500 MPa	1500 MPa	15 MPa	3500 MPa	350 MPa	35 MPa	0.35 MPa	35 MPa	0.35 MPa	3500 MPa	35 MPa	0.35 MPa
μ_i	2	2	2	1.2	1.2	1.2	1.2	1.2	1.2	1.2	1.2	1.2
μ_d	0.8	0.8	0.8	0.6	0.6	0.6	0.6	0.6	0.6	0.6	0.2	0.6
T_m	1500 K	1500 K	1500 K	1393 K	1393 K	1393 K	1393 K	1393 K	1393 K	1393 K	1393 K	1393 K
ξ	1.2	1.2	1.2	1.2	1.2	1.2	1.2	1.2	1.2	1.2	1.2	1.2
Y_{to}	−10 MPa	−150 MPa	−0.1 MPa	−1 MPa	−0.1 MPa	−0.01 MPa	−0.1 kPa	−0.01 MPa	−0.1 kPa	−1 MPa	−0.01 MPa	−0.01 MPa
P_{bd}	1230 MPa	1765 MPa	12.30 MPa	−2940 MPa	−294 MPa	29.4 MPa	0.29 MPa	29.4 MPa	0.29 MPa	−2940 MPa	0.452 MPa	0.452 MPa
P_{bp}	2350 MPa	2880 MPa	23.5 MPa	4100 MPa	410 MPa	41 MPa	0.41 MPa	41 MPa	0.41 MPa	4100 MPa	0.565 MPa	0.565 MPa
G	25 GPa	25 GPa	25 GPa	30 GPa	30 GPa	30 GPa	30 GPa	30 GPa	30 GPa	30 GPa	30 GPa	30 GPa
K_o	37.716 GPa	37.716 GPa	37.716 GPa	45 GPa	45 GPa	45 GPa	45 GPa	45 GPa	45 GPa	45 GPa	45 GPa	45 GPa
Y_c	0.0 MPa	0.0 MPa	0.0 MPa	0.0 MPa	0.0 MPa	0.0 MPa	0.0 MPa	0.0 MPa	0.0 MPa	0.0 MPa	2.5 kPa	2.5 kPa
D_{so}	0	0	0	0	0	0	0	0	0	0	1	1
D_{to}	0	0	0	0	0	0	0	0	0	0	1	1
η	no AF	no AF	no AF	no AF	no AF	no AF	no AF	8.96e7 Pa s	8.96e7 Pa s	8.96e7 Pa s	no AF	no AF
t_{off}	no AF	no AF	no AF	no AF	no AF	no AF	no AF	75 s	75 s	75 s	no AF	no AF
C_{vib}	no AF	no AF	no AF	no AF	no AF	no AF	no AF	0.25	0.25	0.25	no AF	no AF
τ	no AF	no AF	no AF	no AF	no AF	no AF	no AF	22.4 s	22.4 s	22.4 s	no AF	no AF

[a]Strength parameters are defined in Table 1. Note that no AF means no acoustic fluidization.

2.2.1. Comparison With Other Numerical Studies

[11] *Collins et al.* [2004] present the damage accumulation for a terrestrial impact into a granite half-space under lithostatic equilibrium producing a transient crater with a 10 km surface diameter (also called the apparent diameter; it is the diameter of the crater measured at the preexisting surface level). *Collins et al.* [2004] used the shock physics code SALEB in Eulerian mode [*Ivanov and Artemieva*, 2002; *Ivanov and Deutsch*, 1999]. We calculate the same impact conditions using CTH. The strength parameters are chosen to match *Collins et al.*'s [2004] work and are given in Table 2. The shear and tensile strength values are similar in magnitude to those obtained from quasi-static laboratory tests of intact rock [*Lundborg*, 1968; *Pierazzo et al.*, 2005; *Schultz*, 1995]. *Collins et al.* [2004] used an ANEOS equation of state for granite (see appendix of *Pierazzo et al.* [1997]). We conduct simulations with both the ANEOS and a tabular equation of state of granite. For the tabular EOS, we use a density-scaled version (ρ_0 = 2.648 g cm^{-3}) of the CTH Sesame table for α-quartz (the granite EOS is very similar to pure SiO_2), which includes a good treatment of the phase transformation to stishovite, melting, and dissociation [*Kerley*, 1999]. Sesame tables are theoretically based equations of state that are gridded in temperature and density to allow for fast look-up of pressure and internal energy. Differences in the equation of state (ANEOS versus Sesame table) were not important for the level of comparison presented here.

[12] The results of the two simulations are shown in Figure 1. Figure 1a displays the tensile damage (left side) and total damage (right side) 10 s after the impact using CTH, and Figure 1b displays the tensile damage (left side) and total damage (right side) 10 s after the impact as calculated by *Collins et al.* [2004]. The tensile damage and total damage profiles are similar because once the material fails completely in either tension or shear, it is very weak and will likely accumulate damage in the other regime. The maximum resolution of the CTH simulation is 40 cells across the diameter of the projectile. The size of the damaged zone is found to be insensitive to resolution at this level. Acoustic fluidization is not included in the CTH simulation because tests show that adding acoustic fluidization does not significantly change the results for the damage profile at 10 s. We note that, under these impact conditions, using the strength model without acoustic fluidization produces a final crater diameter smaller than predicted by scaling laws (10.4 versus 20.8 km final rim diameter). Including acoustic fluidization in the calculation causes crater collapse to a final complex structure in a manner described by previous workers, with the amount of collapse determined by the acoustic fluidization parameters [*Collins*, 2002; *Collins et al.*, 2004; *Melosh and Ivanov*, 1999; *Wunnemann and Ivanov*, 2003].

[13] The depth and shape of the completely damaged material are very similar in both calculations in Figure 1. Note, however, that the CTH simulation shows a lower amount of damage localization; e.g., the narrow zones of damage in the SALEB calculation are not reproduced. This may partially be a result of damage localization being smeared out as CTH unrefines (increases the cell size) behind the shock wave; however, even with a fixed high resolution mesh we were unable to reproduce the long finger-like extensions of radial damage seen in the SALEB calculation.

[14] The implementation of the strength model described by *Collins et al.* [2004] in CTH produces similar results to their implementation of the model in SALEB. This test provides an excellent validation of similar results obtained with two different shock physics codes.

2.2.2. Comparison With Laboratory Studies

[15] Next, the strength model is used to simulate laboratory-scale impact experiments. *Ai* [2006] and *Ai and Ahrens* [2006] recently performed a series of laboratory cratering experiments to study shock-induced damage during impact

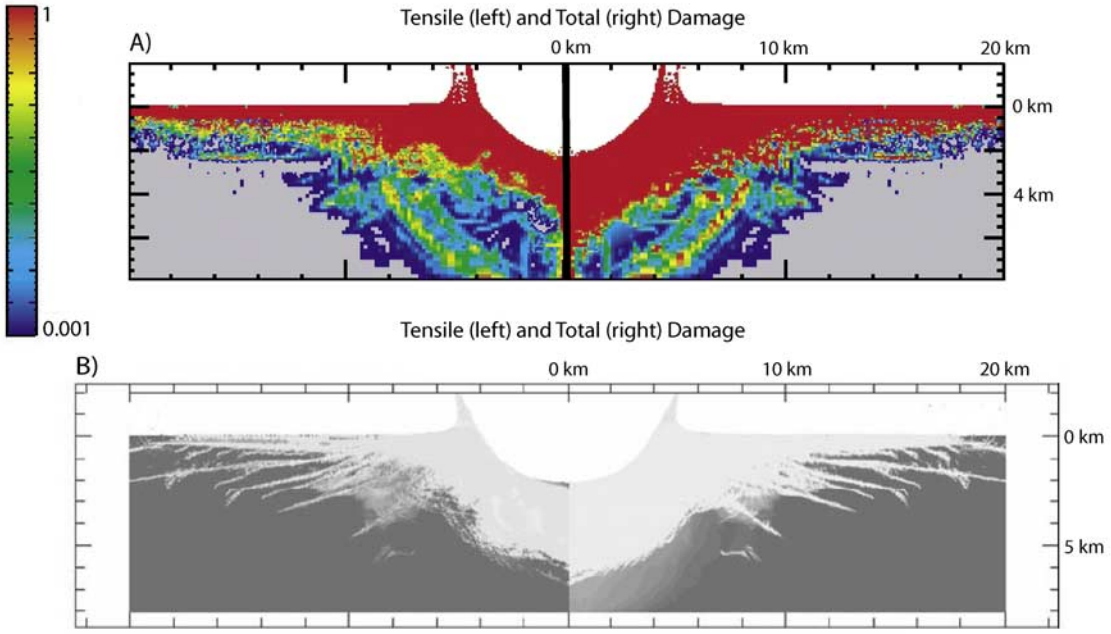

Figure 1. Modeled (left) tensile damage and (right) total damage at 10 s after the vertical impact of a 867-m-radius granite sphere onto a granite half-space at 17 km/s for (a) CTH calculation and (b) numerical results from *Collins et al.* [2004]. In Figure 1b, dark gray is damage equal to 0, and white is damage equal to 1 (reproduced from *Collins et al.* [2004]).

events. We model three of their laboratory experiments in San Marcos granite: impacts by (1) a 0.64-cm-radius copper sphere at 690 m/s (Figure 2); (2) a 3.2-g lead bullet (3 mm radius) at 1200 m/s (Figure 3); and (3) a 0.64-cm-radius lead sphere at 800 m/s (Figure 4). In all cases, the impact is normal to the face of a 20 × 20 × 15 cm unconfined granite block. The strength parameters used for the laboratory cratering experiments in granite are given in Table 2, where the zero-pressure shear and tensile strength, Y_o and Y_{to}, respectively, are an order of magnitude larger than quasi-static strength values. We find that the quasi-static strength parameters used in the simulation above (10-km transient

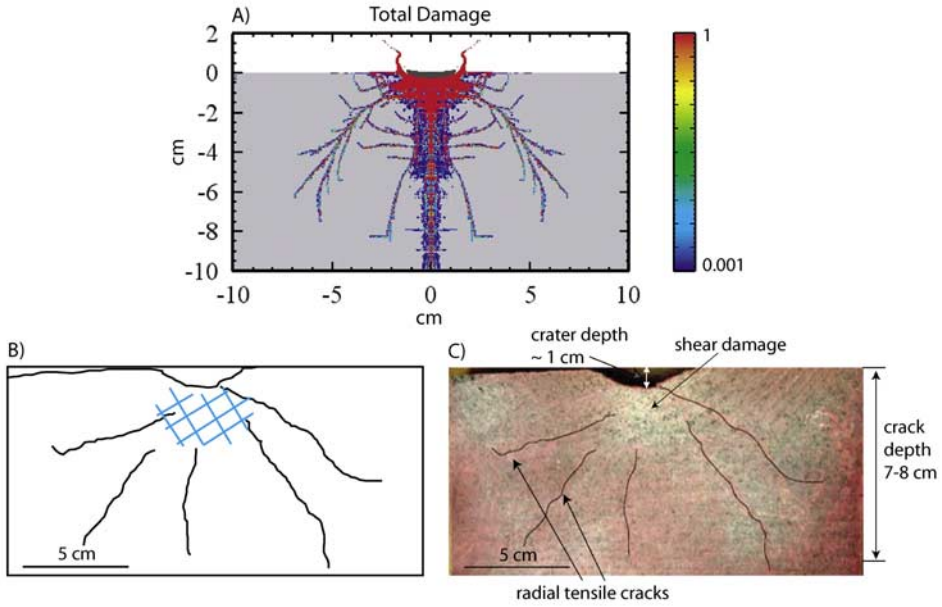

Figure 2. (a) Modeled total damage at 70 s after the vertical impact of a 0.64-cm-radius copper sphere onto a 20 × 20 × 15 cm unconfined granite block at 690 m/s compared with experimental results: (b) sketch and (c) photograph. Radial lines sketched in Figure 2b are tensile cracks; hashed region indicates zone of shear damage. Figure 2c is reproduced from *Ai and Ahrens* [2006].

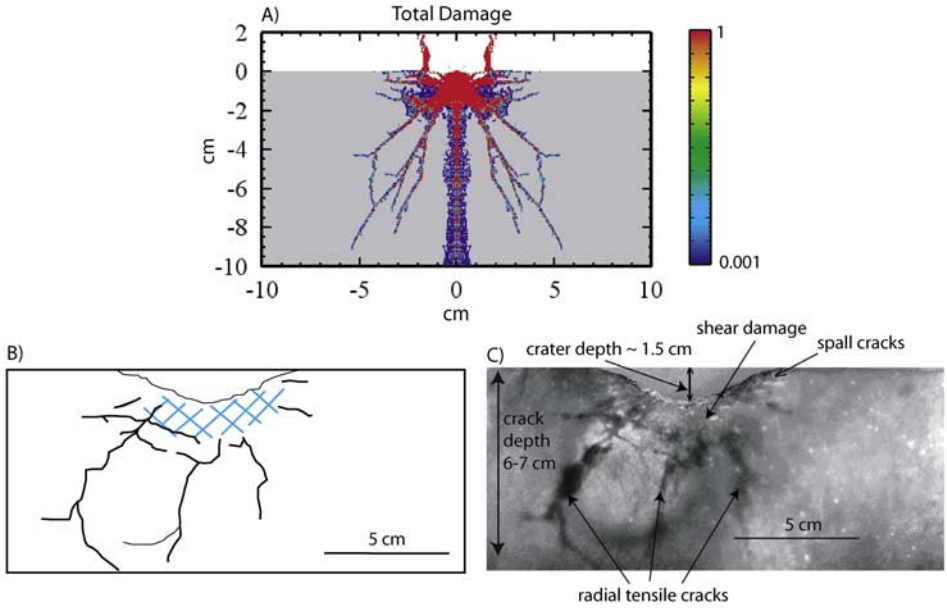

Figure 3. (a) Modeled total damage at 70 s after the vertical impact of a 3.2 g lead bullet onto a 20 × 20 × 15 cm unconfined granite block at 1200 m/s compared with experimental results: (b) sketch and (c) photograph. Radial lines sketched in Figure 3b are tensile cracks; hashed region indicates zone of shear damage. Figure 3c is reproduced from *Ai and Ahrens* [2006].

crater, Figure 1) do not reproduce the radial crack patterns observed in laboratory experiments. The higher strength values for laboratory craters versus quasi-static measurements are primarily the result of the difference in strain rate, which is discussed in section 2.3.

[16] The damaged volume and crack patterns calculated using the strength model in CTH compares very well with the laboratory results for each experiment. All calculated damage profiles were chosen at times when the accumulated damage reaches a plateau. Note that some of the excess damage accumulation along the centerline of the calculations is a numerical artifact resulting from the cylindrical symmetry centerline boundary condition. In the copper impact experiment (Figure 2), *Ai and Ahrens* [2006] observed a hemispherical zone of shear damage of about 4 cm radius, which is similar in shape and size to that produced by the calculation. They also observed radial cracks to depths of about 8 cm. Radial cracks of similar length are also produced in the calculation and are formed by tensile strain localization in the expanding rarefaction wavefront from the impact plane. Furthermore, the model is in good agreement with the number and spacing of radial cracks observed experimentally. In the simulations, the cracks are generated under tensile failure in a homogeneous target by interactions between the expanding rarefaction and compressive shock waves [*Rinehart*, 1968] and do not require the existence of initial flaws. In the natural granite samples used in the laboratory experiments, the exact locations of radial cracks will be influenced by preexisting fractures that accommodate tensile stresses.

[17] In the lead bullet impact experiment (Figure 3), radial tensile cracking is observed to depths of about 6–7

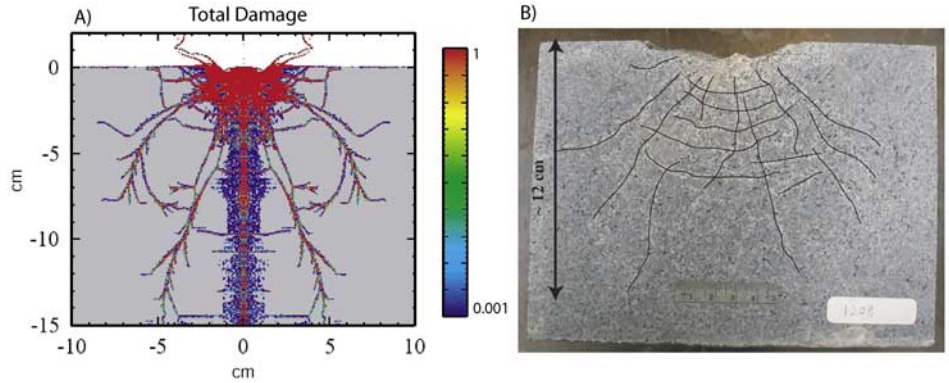

Figure 4. Figure 4a shows the modeled total damage at 100 s after the vertical impact of a 0.64-cm-radius lead sphere onto a 20 × 20 × 15 cm unconfined granite block at 800 m/s compared with experimental results. Figure 4b is reproduced from *Ai* [2006].

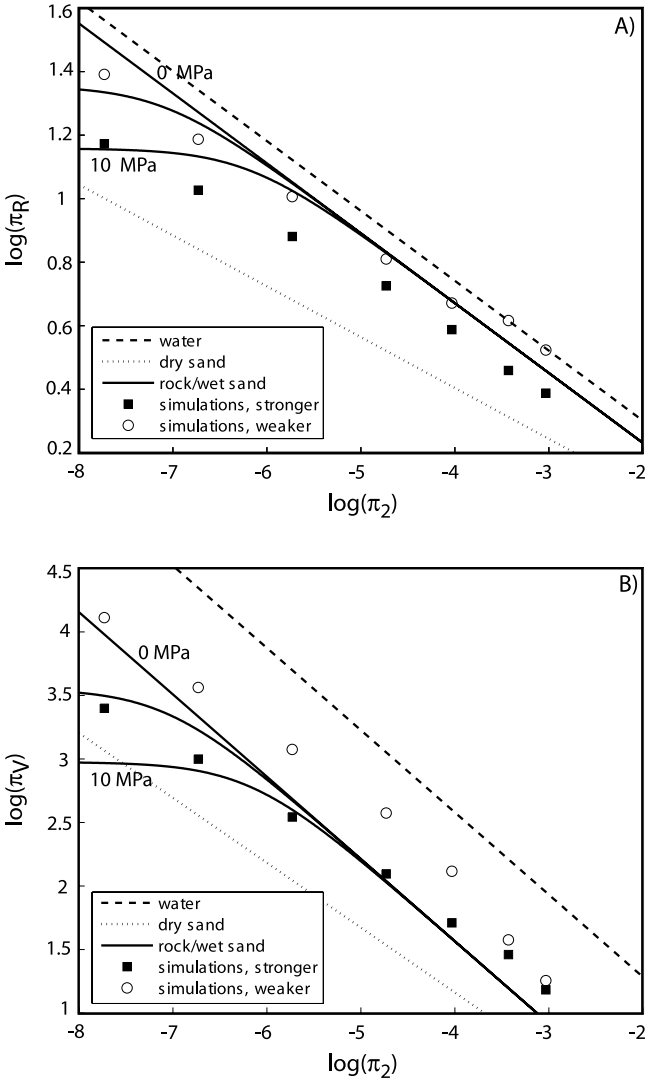

Figure 5. Comparison of transient craters formed under Martian gravity at impact velocities of 10 km/s using CTH simulations (symbols) with π-scaling laws (lines) [*Holsapple*, 1993]. Squares, simulations using laboratory-scale strength parameters; circles, simulations using weaker, planetary-scale strength parameters (see Table 2). Figure 5a shows the ratio of crater surface radius to projectile radius (π_R) versus the inverse Froude number (π_2). Figure 5b shows the cratering efficiency (π_V, ratio of ejected and displaced mass to projectile mass) versus π_2. The dashed line is the scaling law for water, the dotted line is the scaling law for dry sand, and the solid line is the scaling law for wet sand/rock.

centimeters in the experiment, versus 8–9 centimeters in the CTH calculation. The roughly hemispherical zone of shear damage is in good agreement with a radius of 2–3 cm. In the lead sphere impact experiments (Figure 4), the modeled tensile crack pattern agrees well with the experiment; radial cracks extend to about 12 centimeters in the experiment and 12–14 centimeters in the simulation. In addition, both the experiment and the simulation show the development of concentric tensile cracks perpendicular to the radial cracks. The concentric cracks develop after the radial cracks upon arrival of rarefaction waves from the side free surfaces of the granite block (after about 30 μs). The concentric cracks branch from a radial crack and grow to an adjacent radial crack.

[18] The simulations of laboratory experiments shown in Figures 3 through 5 are extremely well-resolved with a maximum resolution of 0.00625 cm in the projectile (approximately 102 cells across the projectile diameter for Figures 3a and 5a) and 0.0125 cm in the target. Tests at higher and lower resolutions showed that the number and spacing of cracks are similar, although the exact position and shape of the tensile cracks changed with resolution. This is unsurprising since crack growth is determined by small stress concentrations, which are sensitive to the maximum resolution of the mesh as well as the adaptive mesh refinement. However, the size of the shear damaged zone, the length of tensile cracks, and the number of tensile cracks were insensitive to resolution at this level.

[19] The strength model is able to accurately reproduce shear and tensile damage beneath laboratory impact craters.

2.2.3. Comparison With Crater Scaling Laws

[20] Several crater scaling laws have been developed to predict the size of a crater on the basis of the impact conditions [*Melosh*, 1989]. The most widely used is π-scaling, which relates nondimensional variables through empirical constants derived from experiments [*Holsapple*, 1993; *Holsapple and Housen*, 2004; *Holsapple and Schmidt*, 1987; *Housen and Holsapple*, 1999; *Schmidt and Housen*, 1987]. The π variables describe transient cratering efficiency and impact energies using the impact parameters and material properties. Crater scaling laws are derived for two regimes: strength-dominated and gravity-dominated cratering events. In the gravity-dominated regime, the crater shape depends on the ratio of the lithostatic stress at a depth of one projectile radius to the normal component of the inertial stress (the inverse Froude number),

$$\pi_2 = \frac{g r_p}{\nu_\perp^2}, \tag{1}$$

where g is the gravitational acceleration, r_p is the projectile radius, and $\nu_\perp$ is the normal component of the impactor's velocity (where $\nu_\perp = \nu \sin\theta$ where θ is the angle of impact from horizontal). In the strength-dominated regime, the crater scaling laws depend on the ratio of some measure of the average shear strength of the target ($\overline{Y}$) to the initial dynamic pressure,

$$\pi_Y = \frac{\overline{Y}}{\rho \nu^2} \tag{2}$$

where ρ is the bulk density of the target (assumed to be equal to the projectile density). For a nondimensional measure of the crater shape, we use the cratering efficiency (π_V, ratio of ejected and displaced mass to projectile mass times a constant factor) and the cubed root of the cratering efficiency times a constant factor (π_R). Note that the constant factors in each case are different and depend on the shape of the crater. π_V is

$$\pi_V = \frac{\rho V}{m_p}, \tag{3}$$

where V is the volume of the transient crater (measured below the preexisting surface) and m_p is the mass of the projectile. If we assume that the crater is parabolic, then

$$V = \frac{\pi H_{st} D_{st}^2}{8}, \tag{4}$$

where H_{st} is the transient crater depth (measured from the surface to the deepest part of the crater at the same time that the transient crater diameter is measured) and D_{st} is the surface diameter of the transient crater. π_R is

$$\pi_R = R_{st}\left(\frac{\rho}{m_p}\right)^{1/3}, \tag{5}$$

where R_{st} is the radius of the transient crater measured at the preexisting surface level. The transient crater radius refers to the widest radius of the crater during excavation. Following *Wunnemann et al.* [2006], we take this point to be when a kink appears in the ejecta curtain. Smooth empirical functions can be written for the dependence of π_R on π_V and π_2 and π_Y that include the transitions between the strength and gravity regimes [*Holsapple*, 1993]:

$$\pi_R = K_R\left[\pi_2\left(\frac{\delta}{\rho}\right)^{1/3} + \pi_Y^{\beta/\alpha}\right]^{-\alpha} \tag{6}$$

and

$$\pi_V = K_V\left[\pi_2\left(\frac{\delta}{\rho}\right)^{1/3} + \pi_Y^{\beta/\alpha}\right]^{-\alpha/3}, \tag{7}$$

where δ is the projectile density, K_R and K_V are experimentally determined constants, and α is related to the experimentally determined coupling exponent, μ, by $\alpha = 3\mu/(2 + \mu)$. For π_R scaling, experimentally determined constants for example materials are water ($K_R = 0.727$, $\mu = 0.564$, and $\overline{Y} = 0$ MPa; no strength), dry sand ($K_R = 0.581$, $\mu = 0.381$, and $\overline{Y} = 0$), and rock ($K_R = 0.619$, $\mu = 0.564$, and $\overline{Y}$ varies depending on the rock strength; approximately 6.9 MPa for strong rock) [*Schmidt and Housen*, 1987; *Holsapple and Housen*, 2004]. For π_V scaling, the experimentally determined constants are water ($K_V = 0.98$, $\mu = 0.55$, and $\overline{Y} = 0$), dry sand ($K_V = 0.132$, $\mu = 0.41$, and $\overline{Y} = 0$), and rock ($K_V = 0.095$, $\mu = 0.55$, and $\overline{Y}$ varies depending on the rock strength) [*Holsapple*, 1993; *Holsapple and Housen*, 2004]. Constructing a scaling law for rock in the gravity regime is difficult primarily due to a lack of data for large-scale cratering events in this material [*Schmidt and Housen*, 1987]. The best approximation to date for the rock scaling law in the gravity regime is the scaling law for wet sand [*Holsapple and Housen*, 2004; *Schmidt and Housen*, 1987], but it is important to note that this approximation has not been experimentally validated.

[21] We compare the strength model results with those expected from π-scaling (Figure 5). Figure 5a shows the results for π_R versus π_2 (in log-log space), and Figure 5b shows the results for π_V versus π_2 (in log-log space). In both plots, the lines represent π-scaling laws; the dashed lines are for water, the dotted lines are for dry sand, and the solid lines are for rock (three different strengths are shown). Simulation results are shown as points. The circles versus the squares represent different choices for the strength parameters (see Table 2). The squares correspond to simulations conducted using strength values similar in magnitude to those measured in quasi-static laboratory tests, while the circles correspond to strength values which are two orders of magnitude lower (Y_o,Y_m, and Y_{to} decreased by two orders of magnitude and P_{bd} and P_{bp} adjusted accordingly; refer to Table 1 and Appendix A for further description of the strength parameters). Note that acoustic fluidization was not included in these calculations, as it has a negligible effect on the size of the transient cavity and acts largely to collapse the transient cavity into a wider and shallower final crater.

[22] In Figures 5a and 5b, each set of simulation results produces linear trends, as predicted from π-scaling. Note that the two largest weaker simulations appear to deviate somewhat from the trend created by the other data points; this is probably because the impacts are large enough, and the target is weak enough, that the crater walls begin to collapse and rebound (note that this is without the aid of acoustic fluidization) before the transient crater is fully formed, making it impossible to accurately measure the transient crater diameter. The data clusters between the predicted results for dry sand and water, indicating that the choice of input parameters for the strength model is reasonable. The weaker simulations produce larger craters than the stronger simulations. This is consistent with *Wunnumann et al.*'s [2006] simulations. *Wunnemann et al.* [2006] conducted numerical simulations with varying values of the coefficient of damaged friction, μ_d. In their simulations, increasing μ_d caused their results to fall progressively further below the π_R values predicted for wet sand, but still between the dry and wet sand scaling lines.

[23] Note that for large-scale impacts into rock, the amount of damage is great enough that crater excavation proceeds chiefly in completely fractured (damage equal to one) rock; this effect was first observed during numerical simulations of asteroids [*Asphaug and Melosh*, 1993; *Nolan et al.*, 1996]. Thus, for large-scale impacts in rocks, the residual strength of the damaged material largely determines the size of the crater. The model implemented here assumes that the strength of damaged material rises linearly with pressure from zero (or some small cohesion value) to the point (pressure) where the damaged strength equals the intact strength with a slope equal to the coefficient of damaged friction, μ_d. Above this pressure, the damaged strength curve follows the intact strength curve (this is based on the belief that at high enough pressures the boundaries between fragments are compressed enough so that they behave like grain boundaries). The intact strength curve is limited by Y_m, the limiting shear strength as pressure increases. Thus, for large-scale impacts, the two most important parameters in determining crater size are μ_d and Y_m; hence increasing or decreasing these will change

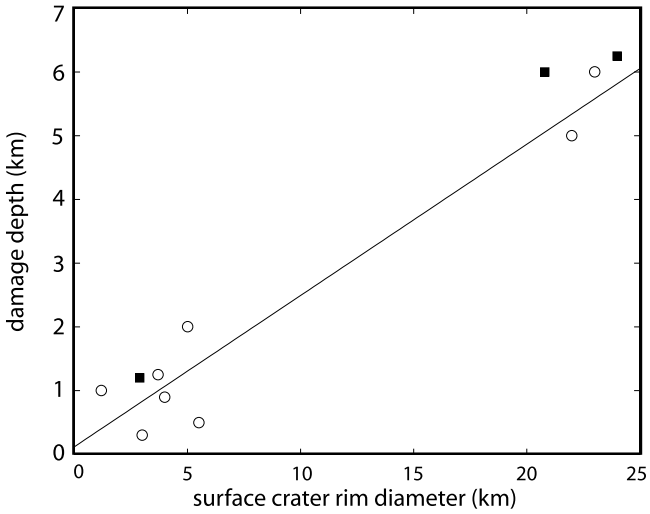

Figure 6. Depth of completely damaged zone (measured from the pre-impact surface) versus final crater rim diameter for strength model results (squares, from simulations which are shown in Figures 1a, 9a, and 10a) compared with measurements from terrestrial craters (circles and fitted black line, from *Ahrens et al.* [2001]).

the crater size, while increasing or decreasing other parameters will have relatively little effect.

[24] The simulations do not match up exactly with the π-scaling predictions. Three inconsistencies in particular are noted. (1) π-scaling predicts that, in the gravity regime, strength should not affect the crater size. Despite this, we find that the weaker simulations produce larger transient craters. However, it should also be noted that the difference between the stronger and weaker simulations does appear to diminish somewhat as crater size increases. (2) The crater shapes predicted by the simulations do not agree with those predicted by standard π-scaling. To see this, note that in Figure 5a, the predicted values of π_R for the weaker simulations fall almost exactly on the π-scaling line for wet sand/rock. Yet the values of π_V for the same simulations are larger than predicted (Figure 5b): the corresponding crater volumes are too large. Note that π_R and π_V are mathematically the same, except for a cube-root and a constant factor, which will depend on the shape of the crater. The coefficients for the π_R and π_V scaling laws are independently fitted to laboratory data using different measurements (diameter and volume, respectively). Thus it appears that the crater shapes produced by our simulations are not self-similar to those produced in the laboratory. (3) Note for targets with strength, the scaling curves should flatten out at small values of π_2 (π_R and π_V should become independent of π_2; this is the strength regime). However, the simulations show little flattening out in what should be the strength regime (note that the smallest crater shown is approximately 25 or 40 m in transient crater surface diameter, depending on the strength). *Holsapple* [1993] notes that the transition between the strength and gravity dominated regimes spans two decades, so it is possible that the simulations are simply not small enough to reach the strength regime. Additionally, it is possible that at this scale, the crater is still large enough that a significant damaged zone is created in which crater excavation can proceed, reducing the apparent strength. Note finally that it is extremely difficult to model the size of very small (laboratory-scale) craters because at this scale, crater size and shape are determined primarily by spall fractures, which are strongly influenced by preexisting flaws. In general, the inconsistencies discussed above suggest that either (1) the strength model is incomplete and/or (2) the scaling laws are incomplete or too simplified to capture the physics of large crater formation. These issues should be investigated more completely in the future.

2.2.4. Comparison to Field Observations

[25] A strong constraint on the accuracy of a model of rock rheology and damage are field observations of seismic velocities beneath terrestrial impact craters. Seismic velocity reflections can be used to determine the depth of intensely cracked rock beneath a crater (corresponding to a damage value of one in the strength model). *Ahrens et al.* [2001] found a linear relationship between damage depth and crater diameter. In Figure 6, we plot calculated depths of completely damaged material using the strength model versus final rim diameters predicted by scaling laws. Note that we use the final rim diameters predicted by π-scaling and collapse laws (H. J. Melosh, Crater Scaling Program, 1998, available at http://www.lpl.arizona.edu/tekton/crater.html) instead of those that result from the simulations because not all of the simulations included acoustic fluidization (and thus do not collapse to wide enough diameters). While adding acoustic fluidization will change the final crater diameter, it will not significantly affect the depth of damage accumulation. Calculated depths of completely damaged material using the strength model are in excellent agreement with the estimated depth of damaged zones beneath similarly sized terrestrial craters.

[26] In summary, these tests have shown that the constitutive model is able to accurately simulate the dynamic rheology of rocks during impact events over a large range of sizes.

2.3. Choosing Strength Parameters

[27] We find that when choosing strength parameters for an impact simulation, the following factors should be considered in addition to the intrinsic material properties: scale, strain rate, and preexisting weaknesses in the target. At the current time, these factors are not explicitly included in the model; thus strength parameters should be carefully chosen in light of the application and the model should eventually be extended to include these effects, as noted in Appendix A.

2.3.1. Scale Effects

[28] Laboratory studies demonstrate that the tensile strength (Y_{to}) of a rock decreases with increasing scale. For example, *Housen and Holsapple* [1999] found that the static tensile strength of granite cylinders increases by a factor of about one and three quarters from a sample volume of 1 cm^3 to 1000 cm^3. A theory for this effect has been developed on the basis of the assumption that all solids contain some inherent distribution of flaws (microcracks, grain boundaries, holes, etc.); this theory can successfully predict the outcome of laboratory collisional disruption

events on the basis of a measured inherent flaw distribution [*Grady and Kipp*, 1980; *Griffith*, 1920; *Holsapple*, 1993; *Housen and Holsapple*, 1990, 1999]. During tensile failure, the most critically stressed flaw will grow and prevent the growth of other flaws. Because the tensile stress required to activate a flaw is inversely proportional to the square root of the length of the flaw, larger flaws are generally the most critically stressed. Thus larger samples will exhibit lower tensile strengths since they are expected to contain larger flaws. If it is assumed that that size of the largest flaw is proportional to a linear measure of the specimen size, then the strength varies as the inverse of the square root of the specimen size [*Housen and Holsapple*, 1999].

[29] Experimental studies have also been conducted to determine the change in shear strength with scale; these studies generally agree that the unconfined uniaxial compressive strength (strength when $\sigma_1 > \sigma_2 = \sigma_3 = 0$, where the σ's are the principal stresses, and stress is positive in compression) decreases with size [*Bieniawski*, 1968; *Dey and Halleck*, 1981; *Jaeger and Cook*, 1976; *Lockner*, 1995; *Paterson*, 1978; *Pratt et al.*, 1972; *Schultz*, 1995; *Shimada*, 1993]. This decrease is up to about an order of magnitude. For example, *Bieniawski* [1968] found that the uniaxial compressive strength of cubes of coal decreased by a factor of 7 from 1 ft sized cubes to 5 ft sized cubes, leveling out at sizes greater than 5 ft. Similarly, *Pratt et al.* [1972] saw an approximately order of magnitude decrease in the strength of quartz diorite as the sample size was increased from 2 in to 9 ft; they also noted a leveling out in the strength for specimens above about 3 ft. However, because shear strengths are technically harder to measure in the laboratory than tensile strengths, the data is limited and somewhat ambiguous; occasionally, the shear strength was found to be relatively constant, or even to increase slightly, with increasing size [*Paterson*, 1978]. Additionally, *Lockner* [1995] noted that the size effect seems to be greater for weaker rocks. A generalization of these experimental results is also prohibited by a lack of agreement concerning a theoretical model for the dependence of shear strength with size. Using a weakest flaw argument similar to that given for tensile strength scale dependence appears not to work [*Brown*, 1971; *Paterson*, 1978]. Finally, there has been very little study of the effect of scale on shear strength for nonzero confining pressures. *Barton* [1976] suggests that a reduced number of pores and flaws at high pressures may reduce the scale effect at higher pressures, but there is little data with which to test this theory. *Singh and Huck* [1973] give some data to confining pressures up to 69 MPa; however, the data is too sparse and at too low pressures to draw any conclusions [*Shimada*, 1993; *Singh and Huck*, 1973]. Thus, while it is clear that Y_o should scale with size (although the extent of the scaling is uncertain), it is unclear whether or not Y_m should also.

2.3.2. Strain Rate Effects

[30] Many laboratory studies have established that tensile strength increases with strain rate; dynamic tensile strengths measured in laboratory shock experiments (strain rates of about 10^4 to 10^6 s^{-1}) can be more than an order of magnitude greater than the tensile strengths measured in quasi-static and low strain rate laboratory experiments (strain rates of about 10^{-5} to 10^0 s^{-1}) [*Ahrens and Rubin*, 1993; *Ai and Ahrens*, 2004; *Grady and Hollenbach*, 1979; *Grady and Lipkin*, 1980]. As for the decrease in tensile strength with scale, this can be explained by the existence of inherent flaws. At high strain rates, the large flaws do not have as much time to grow, and smaller flaws also need to be activated; this effectively increases the strength of the material. Hence tensile strength values are larger for laboratory impact experiments than for planetary-scale impacts. An additional complicating factor is that for planetary-scale impacts, the duration of loading may be more important than the instantaneous strain rate, although this produces qualitatively the same result as observed in laboratory experiments utilizing a constant strain rate to failure (longer duration of loading corresponds to weaker strength) [*Housen and Holsapple*, 1999]. If a simulation produces tensile failure over a large range of strain rates, then the model should explicitly include rate-dependent tensile strength [*Housen and Holsapple*, 1999].

[31] Shear strength has also been observed to increase with strain rate. Laboratory tests have shown that rocks will exhibit brittle failure at low temperatures and stresses if the strain rate is slow enough; this is attributed to "subcritical" (at levels below the failure strength) crack growth [*Lockner*, 1993, 1995]. Additionally, material failing in the ductile regime should also show a strain rate dependence since plastic deformation mechanisms generally depend upon the strain rate [e.g., *Poirier*, 2000]. Finally, we also note that under shock deformation in the laboratory, the maximum shear stress under uniaxial strain (the Hugoniot Elastic Limit) is about two orders of magnitude greater than quasi-static laboratory values for shear strength.

[32] Recall that in the modeling of laboratory experiments discussed above, Y_{to} and Y_o had to be increased by approximately an order of magnitude in order to reproduce observed cracking effects; this necessary adjustment can be attributed to strain rate effects.

2.3.3. Preexisting Weaknesses

[33] Any preexisting weaknesses (for example, regional jointing or faults) will further decrease the target strength and can be accommodated by initializing a calculation with nonzero damage and/or decreasing other strength parameters.

2.3.4. Planetary-Scale Impacts

[34] To summarize, Y_{to} and Y_o are scale and strain rate dependent and Y_m is strain rate dependent and probably not scale dependent (although we do not know for sure). Also, any preexisting weaknesses may weaken the target. Because of these various factors, it is difficult to apply strength values determined in laboratory quasi-static experiments to planetary-scale impact events. In such an event, (1) the scale will be much larger than in the laboratory, (2) the strain rate will be intermediate (higher than in most quasi-static laboratory tests and lower than in most dynamic laboratory tests), and (3) there will likely be more preexisting weaknesses in the target. Point 1 will tend to decrease strength values from those measured in quasi-static laboratory tests, while point 2 will tend to increase strength values. Note that point 3 can be accommodated by initializing a target with nonzero damage. Estimating the relative magnitude of the effects, however, is difficult due the paucity of data and the complexity of the effects. Furthermore, recall that for a planetary-scale impact theimportant parameters in determining the size of the crater appear to be Y_m and μ_d (see the

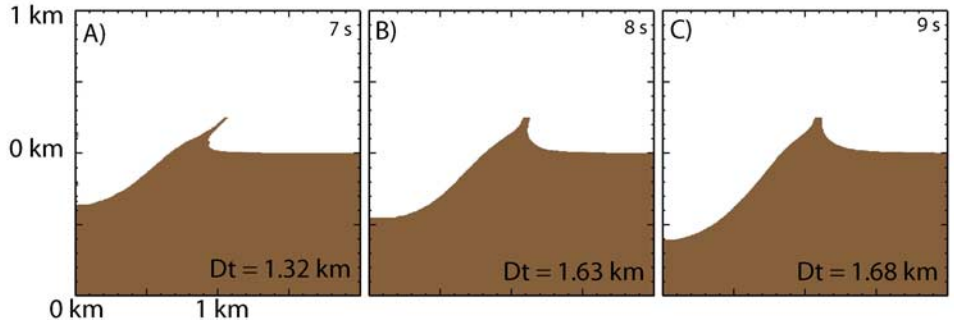

Figure 7. Comparison of transient craters formed by impact into a homogeneous basalt target with varying strengths. The centerline of the calculation is along the left vertical axis. Figure 7a is the strongest target, Figure 7c is the weakest target, and Figure 7b is intermediate. The impactor is a 100-m-diameter basalt asteroid impacting vertically at 17 km/s on the Earth. D_t is the transient crater diameter. The top of the ejecta curtain was clipped to decrease the calculation times.

discussion in section 2.2.3). Thus variations in Y_{to} and Y_o due to scale and strain rate may be relatively unimportant at this scale because crater formation proceeds in a damaged target. On the other hand, variations of Y_m due to strain rate may be significant; this should be investigated further in the future.

[35] To illustrate how changing strength parameters may result in a change in crater shape, we show examples of terrestrial craters formed with varying strengths. Figure 7 displays the transient craters produced by the vertical impact of a 17 km/s, 100-m-diameter basalt asteroid onto a basalt target for three different target strengths. The strength parameters used are shown in Table 2. In Figure 7a, the strength parameters are taken from *Pierazzo et al.* [2005] and are based on fits to laboratory quasi-static triaxial test data. In Figure 7b, the strength is taken to be one order of magnitude lower than the laboratory data (Y_{to}, Y_o, Y_m all decreased by an order of magnitude and P_{bd} and P_{bp} adjusted accordingly), while in Figure 7c, the strength is two orders of magnitude lower. As strength decreases, the crater diameter and depth increase (although, given the two orders of magnitude variation in strength, the change in size is relatively small). Also note that the angle of the ejecta blanket with the preexisting surface changes with strength; as strength is decreased, this angle increases. These results also hold for larger craters that are well within the gravity regime; Figure 8 displays the transient craters produced by the 17 km/s vertical impact of a 1-km-diameter basalt asteroid onto a basalt target for the same three different target strengths.

[36] On the basis of the above discussion of how scale, strain rate, and preexisting weaknesses affect strength, it is clear that using laboratory measured strength parameters for planetary-scale impact events is an over-simplification. However, due to the uncertainties in the magnitude of these effects over the range of interest, as well as uncertainties in π-scaling laws for large impact events (discussed above), picking appropriate strength parameters is very difficult and a range of strength parameters seems to produce reasonably sized transient craters.

3. Layering Effects

[37] We have conducted simulations into layered targets with different strength configurations in order to understand the effects that strength layering can have on the impact cratering process and the final crater morphology. To illustrate these effects, we will present two examples: (1) a

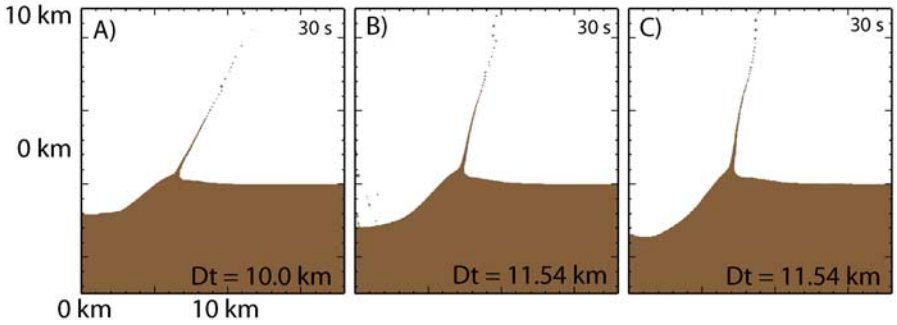

Figure 8. Comparison of transient craters formed by impact into a homogeneous basalt target with varying strengths. Figure 8a is the strongest target, Figure 8c is the weakest target, and Figure 8b is intermediate. The impactor is a 1-km-diameter basalt asteroid impacting vertically at 17 km/s on the Earth. D_t is the transient crater surface diameter.

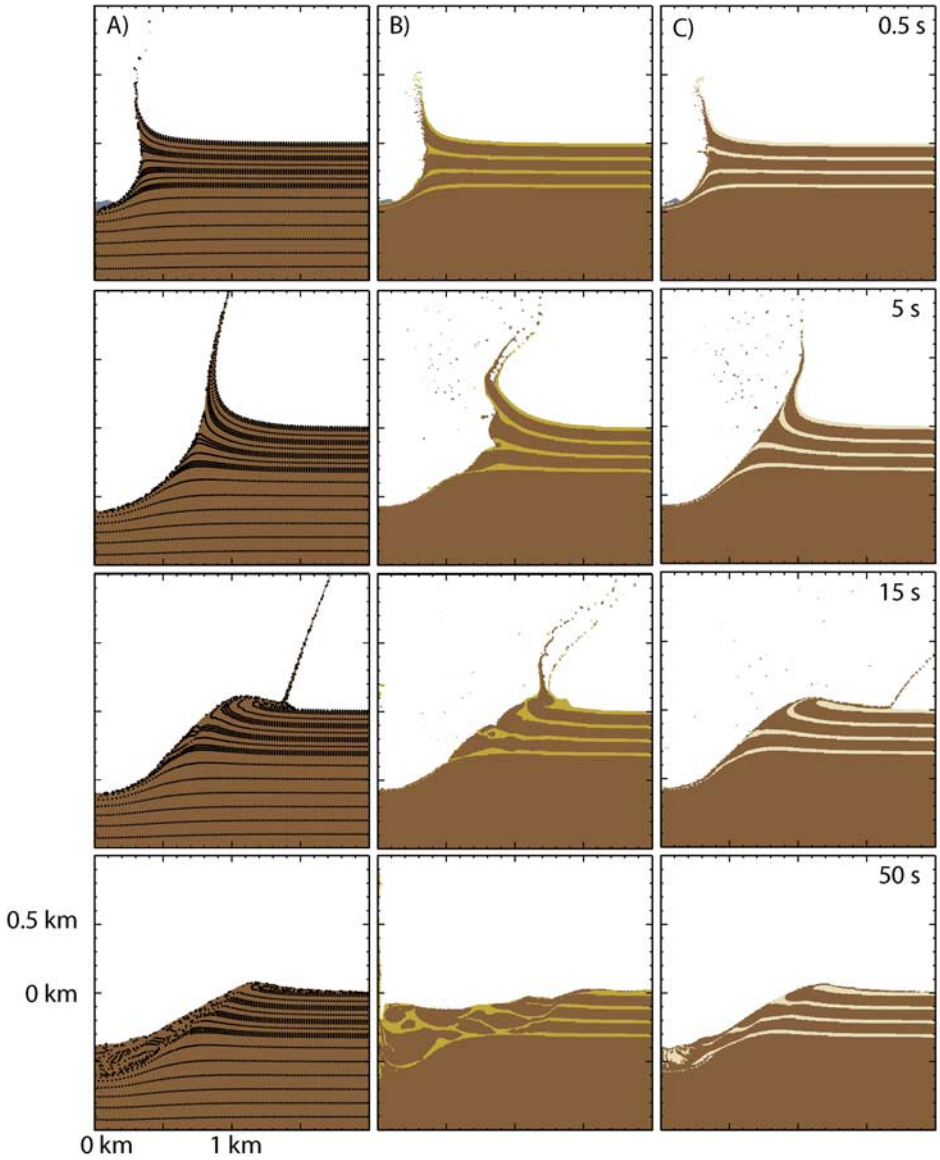

Figure 9. Comparison of simple crater formation in (a) a homogeneous basalt target, (b) a target with weak basalt layers, and (c) a target with strong basalt layers. The impactor is a 100-m-diameter basalt asteroid impacting vertically at 17 km/s on the Earth. Thin layers are 25 m thick; thick layers are 75 m thick. Dark color represents "normal" strength basalt, medium color represents "weak" basalt, and light color represents "strong" basalt. Black dots in Figure 9a are massless Lagrangian tracer particles (in initially horizontal layers), showing structural deformation.

100-m-diameter impactor on the Earth (simple crater regime; predicted surface transient diameter of 1.85 km and final rim diameter of 2.89 km from π-scaling) and (2) a 1-km-diameter impactor on the Earth (complex crater regime; predicted surface transient diameter of 11.2 km and final rim diameter of 24 km from π-scaling). The impacts occur at a characteristic impact velocity for asteroids onto the Earth, about 17 km/s [*Bottke et al.*, 1994].

3.1. Simple Crater

[38] We conduct simulations of a simple crater (100-m-diameter basalt projectile) forming in a basalt target with three different layered strength configurations: (1) a homogenous strength target (Figure 9a), (2) a target with thin (25-m-thick) weak layers (Figure 9b), and (3) a target with thin (25-m-thick) strong layers (Figure 9c). The maximum resolution of the simulations is 2.5 m (40 cells across the projectile diameter, 10 cells across the thin layers). For the basalt equation of state, the CTH basalt Sesame table was used; this equation of state is a density-scaled version of the table for α-quartz [*Kerley*, 1999]. No acoustic fluidization was included because there is a negligible contribution to the final shape of simple craters (see Table 2).

Table 3. Final Crater Dimensions for Simulations Shown in Figure 9

	Figure 9a	Figure 9b	Figure 9c
Surface diameter, km	1.94	2.75	1.86
Surface depth, m	380	120	400
Surface depth/surface diameter ratio	0.20	0.04	0.22

[39] For the homogenous strength target case (case 1), the strength parameters were chosen to be two orders of magnitude weaker than in quasi-static laboratory tests of basalt (Y_o, Y_m, and Y_{to} decreased by two orders of magnitude and P_{bd} and P_{bp} adjusted accordingly) and are meant to represent an average or normal basaltic planetary surface (in terms of quasi-static strength values, these values correspond roughly to a highly weak and weathered sedimentary rock). This stress degradation was applied in order to obtain transient crater diameters of the size predicted by π-scaling. Since our results showed inconsistencies with π-scaling and π-scaling for rocks at large scales is itself uncertain (discussed in section 2.2.3), this may or may not be the best approach. Note the same goal could also be achieved by decreasing μ_d (see section 3.3). While the details of a specific cratering event will depend on the exact strength chosen as well as the size, position, and strength difference between layers, our goal here is simply to qualitatively illustrate some of the possible effects of layering and to emphasize that these effects can be observationally significant.

[40] The weak layers (case 2) are taken to be two orders of magnitude weaker (Y_o, Y_m, and Y_{to} decreased by two orders of magnitude and P_{bd} and P_{bp} adjusted accordingly) than the strength of the normal basalt. This is roughly equivalent to going from a strong crystalline rock (such as basalt) to a highly weathered and altered sedimentary rock (such as shale) [*Zhang*, 2005]. The strong layers (case 3) are taken to be two orders of magnitude stronger than the strength of the normal basalt.

[41] The important thing to note from these simulations is the way in which the ejecta curtain structure and final crater morphology vary with the inclusion of weaker layers in the target. For the homogeneous target, the ejecta curtain forms an inverted cone at an angle of about 75 degrees from the surface. With the addition of weak layers, however, the upper weak layer pulls apart from the layer underneath, forming a two-layer ejecta curtain structure (see Figure 9b at 15 s). This two-layer ejecta curtain structure has also been noted in simulations of craters into marine targets [*Ormö et al.*, 2002]. The angle of the ejecta curtain is no longer constant, but varies from vertical (near the surface) to much lower angles (about 45 degrees) further up, creating a curved profile. In addition, the normal strength material in the ejecta curtain pushes the upper weak layer, creating a bulge that flows along the surface ahead of the ejecta curtain. These changes in the ejecta curtain structure are due to variations in the excavation flow in materials with differing strengths and will lead to changes in the final ejecta blanket thickness and profile. During crater collapse, the weaker material collapses and flows more readily than the normal strength material; this results in terraces of more resistant material in the crater wall. Additionally, this extra collapse results in a crater that has a lower depth, greater diameter, and lower rim height (because the weak upper layer flows away from the rim) than for a crater formed in a homogenous target (see Table 3).

[42] The inclusion of stronger layers in the target (Figure 9c) does not produce as many changes as the inclusion of weaker layers. The final crater dimensions for the strong layered target case are similar to those for the homogeneous target case (see Table 3). There are, however, some differences between the ejecta curtain structure for the two cases; the ejecta curtain for the strong layered case forms an angle of approximately 60 degrees from the surface with a kink to higher angles (about 75 degrees) further up.

3.2. Complex Crater

[43] Next, we conduct simulations of a complex crater (1-km-diameter basalt projectile) forming in the same three target configurations (Figure 10). The maximum resolution of the simulations was 25 km in both the target and the projectile (40 cells across the diameter of the projectile and 10 cells across the thin layers). The target strengths are the same as in Figure 9, except that acoustic fluidization was included since the impact falls within the complex crater regime. The acoustic fluidization parameters chosen are shown in Table 2; these parameters were found to produce final crater depths and diameters similar to those predicted by scaling laws. Note that the acoustic fluidization viscosity chosen here is somewhat greater than the values chosen by previous workers [*Collins*, 2002; *Collins et al.*, 2004; *Melosh and Ivanov*, 1999; *Wunnemann and Ivanov*, 2003]. This is because we chose intact strength values that are lower than those chosen by these workers; as discussed previously, this was done in order to produce transient craters and final simple craters with diameters as predicted from π scaling laws. As a first order approximation, normal, weak, and strong strength basalt layers were all taken to have the same acoustic fluidization parameters.

[44] While the ejecta curtain structure was strongly affected by layering in the simple crater case, the ejecta curtain structure for the three complex craters shown in Figure 10 appears to be fairly independent of layering structure; in all cases the ejecta curtain is a smooth inverted cone that forms an angle of about 75 degrees with the surface. However, as in the case for the simple craters, the inclusion of weak layers can significantly change the final crater morphology (see Table 4). This is due to the greater amount of collapse experienced by weaker materials. For the homogenous target (Figure 10a), the crater floor rebounds into a peak and then collapses back, producing a broad, smooth central mound. With the inclusion of weak layers (see Figure 10b), the floor becomes bumpy and irregular. Additionally, the upper weak layer collapses extensively and flows away from the rim; this results in a very indistinct rim and a wider crater.

[45] Including strong layers for the complex crater case (Figure 10c) does not have any significant effects (for the strength parameters chosen). The crater dimensions for the homogeneous case and the case with strong layers are very similar (see Table 4).

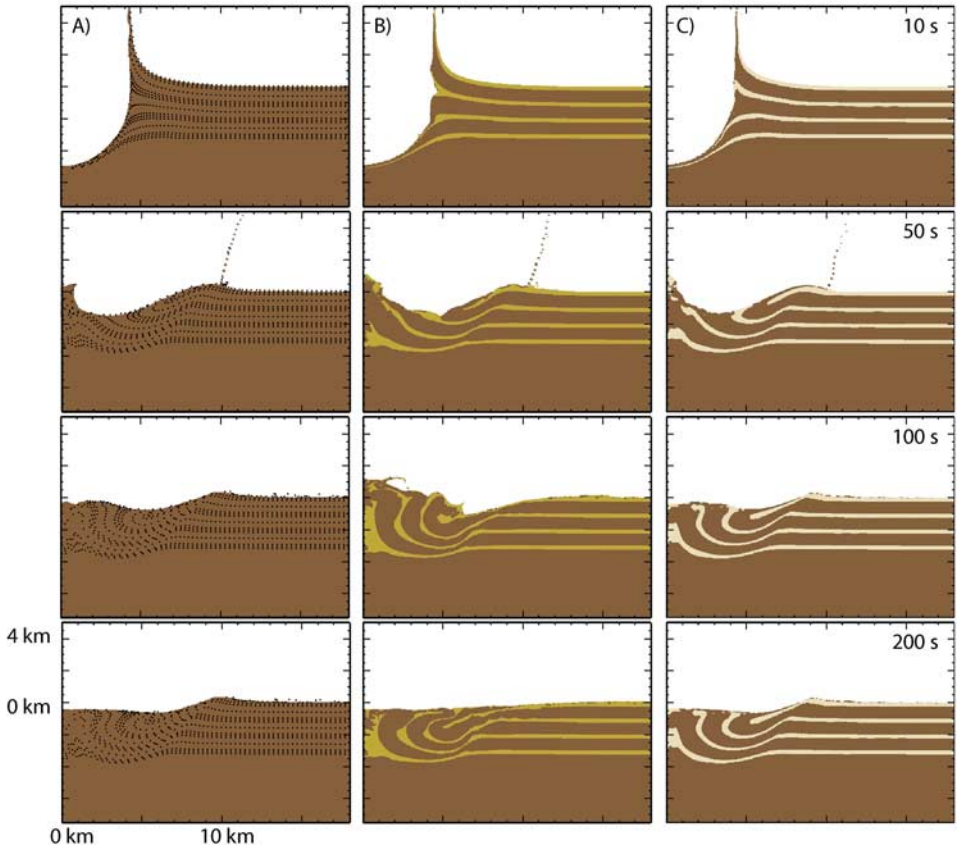

Figure 10. Comparison of complex crater formation in (a) a homogeneous basalt target, (b) a target with weak basalt layers, and (c) a target with strong basalt layers. The impactor is a 1-km-diameter basalt asteroid impacting vertically at 17 km/s on the Earth. Thin layers are 250 m thick; thick layers are 750 m thick. Dark color represents "normal" strength basalt, medium color represents "weak" basalt, and light color represents "strong" basalt. Black dots in Figure 10a are massless Lagrangian tracer particles (in initially horizontal layers), showing structural deformation.

3.3. Regolith Over a Competent Layer: Small Lunar Craters

[46] As an example of how crater morphology can be used to infer subsurface properties, we use the strength model to reproduce the morphologic variations that are observed in small lunar craters by modeling a weak regolith overlying competent rock. These variations were described and reproduced in the laboratory by *Oberbeck and Quaide* [1967] and *Quaide and Oberbeck* [1968] [see also *Melosh*, 1989; *Wilcox et al.*, 2005]. They describe a morphological progression of crater morphology which is dependent upon the ratio of the final rim diameter of the crater, D_r, to the regolith thickness, t. They found that (1) for D_r/t much less than 4, craters show simple bowl shapes (normal morphology), (2) for D_r/t between 4 and 7.5, central mounds form (central mound morphology), (3) for D_r/t between 8 and 10, a flat floor forms (flat floor morphology), and (4) for D_r/t much greater than 10, concentric nested craters form (concentric crater morphology); examples of these crater types are shown in Figure 11. We are able to reproduce these morphologies using numerical simulations. Figures 12 and 13 show the results of a basalt projectile impacting vertically at 17 km/s on the moon for a 10-m-thick regolith (a reasonable value for the moon). The projectile radius was varied to produce craters of differing sizes (projectile size increases from Figures 12a and 13a to Figures 12d and 13d). Note that we simulated vertical impacts only, whereas Quaide and Oberbeck used a range of impact angles. The projectile diameter for the simulation (D_p) and the resulting D_r/t is given in the figures. The competent rock is modeled with the CTH basalt Sesame table equation of state and the same strength parameters as used for the basalt in the previous layering figures. The regolith is modeled using the dry-sand equation of state, which is the α-quartz equation of state with a lower initial density and a pore-

Table 4. Final Crater Dimensions for Simulations Shown in Figure 10

	Figure 10a	Figure 10b	Figure 10c
Surface diameter, km	17.0	25.8	16.5
Surface depth, m	640	430	640
Surface depth/surface diameter ratio	0.038	0.017	0.039

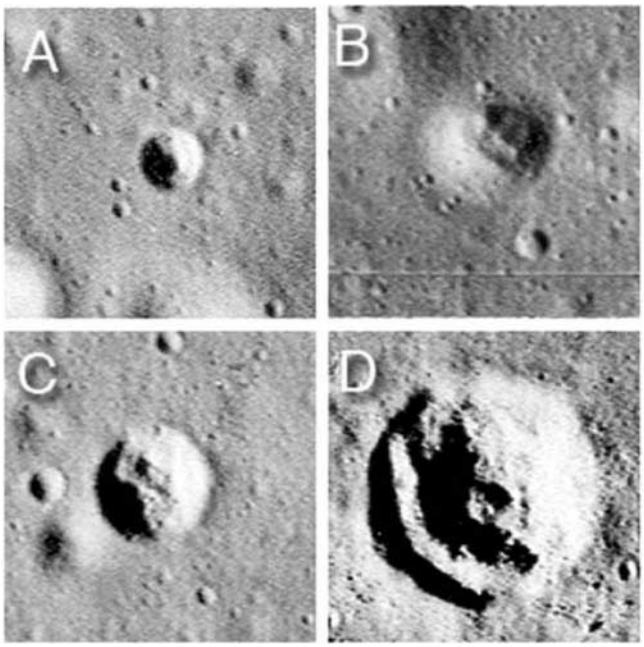

Figure 11. Examples of morphologic variations among small lunar craters: (a) normal, bowl-shaped crater, (b) central mound crater, (c) flat-floored crater, and (d) concentric crater (Lunar Orbiter Image LO3-188-H2, reproduced from *Wilcox et al.* [2005]). Images are all 119 m across.

compaction model (the P-α model) [*Herrmann*, 1969; *Hertel and Kerley*, 1998; *Kerley*, 2002]. The maximum resolution of the simulations was at least 30 cells across the diameter of the projectile. Figures 12 and 13 represent different choices for the strength of the regolith; this will be discussed below. For both strength choices, the morphologic progression described by Quaide and Oberbeck is observed; as the projectile size increases, the crater shape goes from normal bowl-shaped morphology (Figures 12a and 13a), to central mound morphology (Figures 12b and 13b), to flat floor morphology (Figures 12c and 13c), to concentric crater morphology (Figures 12d and 13d). Note that the D_r/t ratios for these simulations do not fall exactly within the boundaries between the varying crater types as determined by *Quaide and Oberbeck* [1968]. For example, in Figures 13b and 13c, the crater diameter actually decreases even though the impactor is larger and the correct morphologic progression (from central peak to flat floor) is observed. The exact transition between boundaries may be affected in part by the simulation resolution and/or the substrate strength. *Quaide and Oberbeck* [1968] found that the boundary positions changed with the strength of the substrate; in particular, the boundary between concentric crater morphology and flat floored crater morphology was observed to vary the most: D_r/t ratios at the boundary ranged from 8 to 10 when the unconfined compressive strength of the substrate was varied from 1.5 bars to 2060 bars (0.15 MPa to 206 MPa).

[47] The strength parameters used to model the regolith are shown in Table 2; the underlying competent rock is assumed to have the same strength as the normal basalt in the previous sections. The initial shear (D_{so}) and tensile (D_{to}) damage of the regolith were taken to be one because the regolith is a completely predamaged granular material. The cohesion chosen is similar to values determined from measurements of the lunar regolith [*Gromov*, 1998; *Holsapple and Housen*, 2007; *Mitchell et al.*, 1972]. Other strength parameters were initially taken to be the same as the underlying basalt; however, we found that the strength

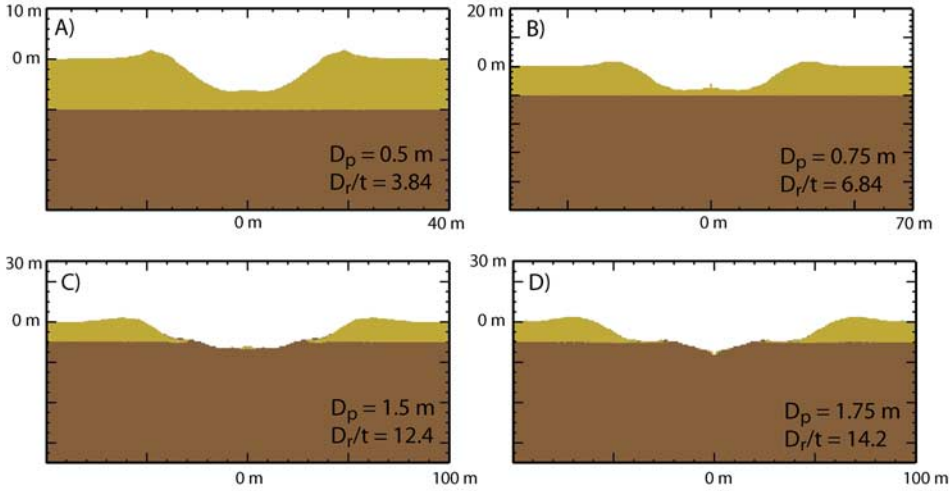

Figure 12. Final crater shapes for impacts into a target with a 10-m-thick regolith over a competent substrate. The impactor is a basalt asteroid impacting vertically at 17 km/s on the Moon; the impactor diameter (D_p) was varied to produce different size craters. The ratio of the final rim diameter (D_r/t) to the regolith thickness results in different crater morphologies: (a) normal, bowl shape, (b) central mound, (c) flat floor, and (d) concentric crater. The strength of the regolith is modeled by decreasing Y_m, the limiting strength at high pressure, from substrate values.

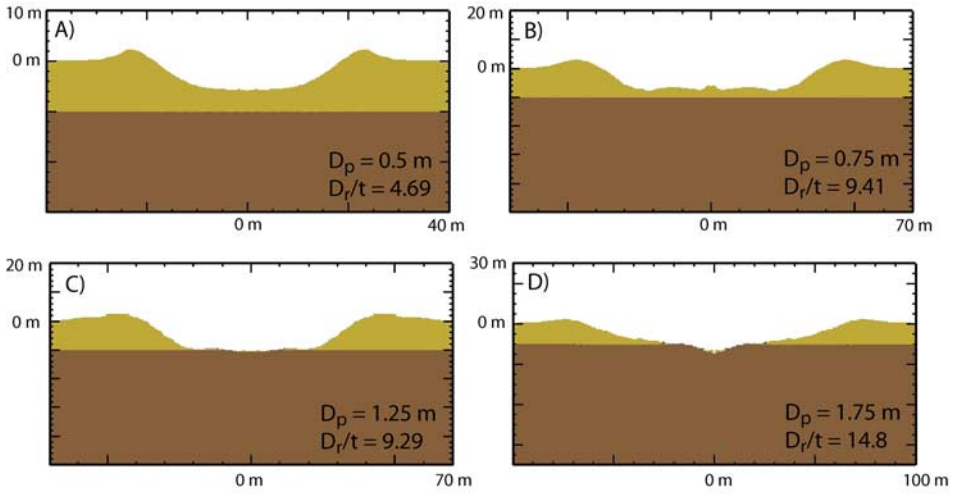

Figure 13. Same as Figure 12 except the strength of the regolith is modeled by decreasing μ_d, the coefficient of damaged friction, from substrate values.

of the regolith had to be further reduced in order to form concentric craters. This can be done by either (1) decreasing Y_m (Figure 12; Y_m was reduced by two orders of magnitude relative to the substrate) or (2) decreasing μ_d (Figure 13; μ_d was reduced from the substrate value of 0.6 to 0.2). Note that for a reasonable range of strengths, the absolute strength is negligible compared to the strength difference: as long as there is a sufficient difference in strength between the regolith and the underlying surface, the same morphological progression of crater morphology will be achieved (although it will take projectiles with more kinetic energy to produce similar looking craters when the strength is greater). In summary, by choosing appropriate strength parameters (the strength of the regolith must be significantly weaker than the underlying competent rock), we are able to reproduce the morphologies of small lunar craters using the strength model.

4. Conclusions

[48] We have implemented the rheologic model for geological materials described by *Collins et al.* [2004] into the shock physics code CTH. We demonstrate that a single model is able to produce reasonably shaped impact craters and damaged zones over a wide range of length scales, from laboratory size craters to complex craters on planetary surfaces, when the appropriate strength parameters are chosen. The model relies upon bulk material properties for input parameters. Additional effects on strength (not included in the model), such as scale and strain rate dependence, are important in some situations. These effects should be investigated further in the future.

[49] Using the updated code, idealized calculations of layered surfaces demonstrate that contrasting strength layers have significant effects on the ejecta curtain structure and the final crater morphology produced by an impact. Hence observed crater morphologies may be used to infer the material properties of widespread subsurface layers on planetary surfaces. As an example, we reproduce the morphologic variations seen in small lunar craters by modeling a regolith overlying competent rock.

[50] With the development of more realistic rheologic models in shock physics codes and agreement between different codes (e.g., this work and *Collins et al.* [2004]), studies of the impact cratering record may provide more detailed information about the material properties and structure of planetary surfaces.

Appendix A: Strength Model Description

[51] We implemented the strength model described by *Collins et al.* [2004]; precursor work to their model was conducted by *Ivanov et al.* [1997]. A detailed description of the model can be found in these papers; however, for the purpose of discussing specific model parameters, we reproduce the equations here. In CTH, the model is named the ROCK model to distinguish it from other existing models in the code.

[52] The strength model takes the current state (temperature, pressure, stress, and strain rate) of the material in a computational cell and returns the updated deviatoric stress tensor. The computational steps are as follows:

[53] 1. Calculate the limiting tensile strength of the cell according to

$$Y_t = Y_{to} * F_{therm} * (1 - D_{tot}) \tag{A1}$$

$$F_{therm} = \tanh\left[\xi\left(\frac{T_m}{T} - 1\right)\right] \tag{A2}$$

where Y_t is the limiting tensile strength, Y_{to} is the maximum tensile strength, F_{therm} is a thermal degradation factor, D_{tot} is the total damage, ξ is a material constant, T_m is the melting temperature, and T is the temperature. Note that the tensile strength decreases with increasing temperature and total damage; the hyperbolic tangent form for the reduction in strength due to temperature was determined experimen-

tally by *Ohnaka* [1995]. Y_t is the minimum principal stress (where Y_t is negative) that the cell is allowed to have.

[54] In this paper, we demonstrate that a single material constant value for Y_{to} is not appropriate for all applications, and that Y_{to} should be replaced with a function of the length scale and strain rate. In addition, we note that for planetary-scale applications, the pressure dependence upon melting should be accounted for by replacing the single value for T_m with a melting curve.

[55] 2. If there is no acoustic fluidization, then calculate the limiting shear strength of the cell according to

$$Y_i = Y_o + \frac{\mu_i P}{1 + \mu_i P/(Y_m - Y_o)} \tag{A3}$$

$$Y_d = Y_c + \mu_d P \tag{A4}$$

$$Y_s = [Y_i(1 - D_{tot}) + Y_{dD_{tot}}]^* F_{therm} \tag{A5}$$

where Y_i is the shear strength of the intact (total damage equal to zero) rock, Y_o is the shear strength of the intact rock at zero pressure, μ_i is the coefficient of internal friction of the intact rock, P is the pressure, Y_m is the limiting strength as pressure increases (the von Mises strength), Y_d is the shear strength of the completely fragmented (total damage equal to one) rock, Y_c is the zero-pressure cohesion, μ_d is the coefficient of friction of the completely fragmented rock, and Y_s is the shear strength. Note that the shear strength is given as a linear combination of the shear strength of the completely intact and completely damaged rock (depending on the amount of damage), and includes thermal degradation effects. If $Y_d > Y_i$(which occurs when the pressure is sufficiently high), then these equations no longer hold and the shear stress is assumed to follow the thermally degraded intact shear strength, regardless of damage. This is based on the idea that at sufficiently high pressures, damaged rock is thought to behave like intact rock because the boundaries between fragments are so compressed that they behave like grain boundaries. The form of equation (A3) was determined experimentally by *Lundborg* [1968].

[56] In this work, we demonstrate that Y_d should be replaced by a function of strain rate and scale. Additionally, Y_m is strain rate dependent, but probably not scale dependent.

[57] 3. If there is acoustic fluidization [*Collins*, 2002; *Collins et al.*, 2004; *Melosh and Ivanov*, 1999; *Wunnemann and Ivanov*, 2003], then calculate the limiting shear strength of the cell according to

$$Y_s = Y_b + \rho * \eta * \varepsilon_{rate} \tag{A6}$$

$$P_{vib} = \rho * C_s * v_g \tag{A7}$$

where Y_b is known as the Bingham yield strength. This is the yield strength if the pressure were equal to the local pressure minus the vibrational pressure (P_{vib}) (equations (A3) through (A5) where Y_b is substituted for Y_s and $P - \mathrm{P}_{vib}$ is substituted for P). ρ is the density, η is the acoustic fluidization viscosity, ε_{rate} is an invariant measure of the strain rate (specifically, the square root of the second invariant of the deviatoric strain rate tensor; this is chosen to correspond with the yield strength criteria), C_s is the sound speed, and v_g is the vibrational particle velocity. The maximum vibrational particle velocity is assumed to be some fraction (C_{vib}) of the maximum cell velocity ($V_{g,max}$) and to decay exponentially with time (t) according to

$$v_g = v_{g,\max} \exp(-t/\tau) \tag{A8}$$

where τ the acoustic fluidization decay constant. Looking at equation (A6), it is seen that acoustic fluidization will not cause failure of the target material unless the shear stresses exceed Y_b (also known as the Bingham yield stress); above that, the material will flow with an effective viscosity of η.

[58] Note that the four acoustic fluidization parameters are validated through a combination of impact crater scaling laws for the sizes of transient and final crater cavities and observations of final crater shapes. These parameters are dependent on the assumed strength model and must be adjusted when the strength model parameters change.

[59] 4. Calculate the trial deviatoric stresses, assuming that all of the deformation can be accommodated elastically. The shear modulus is degraded according to the same factor (F_{therm}) used to degrade the shear and tensile strength.

[60] 5. Calculate the second invariant, J_2, of the trial deviatoric stress tensor.

[61] 6. Apply the shear failure criteria. If $J_2 > Y_s^2$, then the cell is failing in shear and the deviatoric stresses need to be decremented by a factor of $Y_s/\sqrt{J_2}$.

[62] 7. Apply the tensile failure criterion. If the greatest principal stress of the stress tensor is larger than the tensile yield strength (where tensile stresses are positive), then the cell is failing in tension. In CTH, void space is iteratively added to simulate fracture until the averaged principal tensile stress of the cell is equal to the tensile strength. Note that the model implementation by *Collins et al.* [2004] does not add void upon tensile failure.

[63] 8. Update the total plastic strain in the cell. If the cell is currently failing (in shear, tension, or both), then

$$\varepsilon_{tot} = \varepsilon_{tot} + \varepsilon_{rate}^* dt \tag{A9}$$

where ε_{tot} is the total plastic strain in the cell, ε_{rate} is an invariant measure of the strain rate in the cell, and d_t is the time step.

[64] 9. Increment the shear damage (if the cell is failing in shear) using

$$D_s = D_s + \frac{\varepsilon_{rate}^* dt}{\varepsilon_f} \tag{A10}$$

where D_s is the shear damage, and ε_f is the equivalent plastic strain at failure. ε_f is an increasing function of pressure, such that at low pressures damage will accumulate quickly and the material will behave in a more brittle manner, while at high pressures damage will accumulate slowly and the material will behave in a more ductile manner. The input parameters P_{bd} (brittle ductile transition

pressure) and P_{bp} (brittle plastic transition pressure) govern the pressures at which the transitions between these behaviors (brittle, semi-brittle, and ductile) occur for a given material. The shear damage is limited to one. P_{bd} can be calculated as the intersection of the intact yield surface and the damaged yield surface, while P_{bp} can be calculated as where the pressure is equal to twice the yield strength [*Collins et al.*, 2004; *Evans and Kohlstedt*, 1995; *Goetze*, 1978].

[65] 10. Increment the tensile damage (if the cell is failing in tension) using

$$\frac{dD_{ten}^{1/3}}{dt} = \frac{0.4C_s}{d_{\min}} \tag{A11}$$

where D_{ten} is the tensile damage, C_s is the sound speed, and $d_{\min}$ is the minimum dimension of the cell. Essentially, equation (A11) can be thought of as simple crack growth model, where the crack growth speed is $0.4C_s$ (this is the maximum crack growth speed which is asymptotically approached as the crack grows [see *Myers*, 1994]) and the growth is limited to $d_{\min}$ in a given time step. The tensile damage is limited to one. From this work and *Collins et al.* [2004], it is clear that the shear and tensile damage variables are nearly equal; thus having two damage variables may be unnecessary.

[66] 11. Increment the total damage using

$$D_{tot} = D_s + D_{ten} \tag{A12}$$

where the total damage is limited to a maximum value of one.

[67] **Acknowledgments.** We thank Gareth Collins for helpful discussion and providing us with the iSALE strength model subroutines, which are the combined work of Boris Ivanov, Gareth Collins, Kai Wunnemann, and Jay Melosh. We also greatly appreciate the thoughtful reviews provided by Gareth Collins and Anita Ai, as well as the comments from Jay Melosh. The review by Garth Collins in particular greatly improved the manuscript. L.E.S. was supported by a NDSEG fellowship.

References

Ahrens, T. J., and A. L. Rubin (1993), Impact-induced tensional failure in rock, *J. Geophys. Res.*, *98*(E1), 1185–1203.

Ahrens, T. J., K. Xia, and D. Coker (2001), Depth of cracking beneath impact craters: New constraint for impact velocity, in *The Proceedings of the 12th Topical Conference on Shock Compression of Condensed Matter*, edited by M. D. Furnish et al., pp. 1393–1396, Am. Inst. of Phys., New York.

Ai, H. (2006), Shock-induced damage in rocks: Application to impact cratering, Ph.D. thesis, 178 pp., Calif. Inst. of Technol., Pasadena.

Ai, H. A., and T. J. Ahrens (2004), Dynamic tensile strength of terrestrial rocks and application to impact cratering, *Meteorit. Planet. Sci.*, *39*, 233–246.

Ai, H. A., and T. J. Ahrens (2006), Numerical modeling of shock-induced granite under dynamic loading, in *The Proceedings of the 14th Topical Conference on Shock Compression of Condensed Matter*, edited by M. D. Furnish et al., pp. 1431–1434, Am. Inst. of Phys., Melville, N. Y.

Asphaug, E., and H. J. Melosh (1993), The Stickney impact of Phobos: A dynamical model, *Icarus*, *101*, 144–164.

Barton, N. (1976), The shear strength of rock and rock joints, *Int. J. Rock Mech. Min. Sci. Geomech. Abstr.*, *13*, 255–279.

Belton, M. J. S., and Deep Impact Team (2006), A deep impact mission contribution to the internal structure of Jupiter family cometary nuclei: The talps or "layered pile" model, *Lunar Planet. Sci.*, *XXXVII*, Abstract 1232.

Belton, M. J., et al. (2007), The internal structure of Jupiter family cometary nuclei from deep impact observations: The talps or "layered pile" model, *Icarus*, *187*(1), 332–344.

Beyer, R. A., and A. S. McEwen (2005), Layering stratigraphy of eastern Coprates and northern Capri chasmata, Mars, *Icarus*, *179*, 1–23.

Bieniawski, Z. T. (1968), The effect of specimen size on compressive strength of coal, *Int. J. Rock Mech. Min. Sci.*, *5*, 325–335.

Bottke, W. F., M. C. Nolan, R. Greenberg, and R. A. Kolvoord (1994), Collisional lifetimes and impact statistics of near-Earth asteroids, in *Hazards Due to Comets and Asteroids*, edited by T. Gehrels, pp. 337–357, Univ. of Ariz. Press, Tucson.

Brown, E. T. (1971), Strength-size effects in rock material, paper II-11 presented at Symposium of the International Society of Rock Mechanics: On Rock Fracture, Nancy, France.

Collins, G. (2002), Numerical modeling of large impact crater collapse, Ph.D. thesis, 235 pp., Univ. of London, London.

Collins, G. S., and K. Wunnemann (2005), How big was the Chesapeake Bay impact? Insight from numerical modeling, *Geology*, *33*(12), 925–928.

Collins, G. S., H. J. Melosh, and B. A. Ivanov (2004), Modeling damage and deformation in impact simulations, *Meteorit. Planet. Sci.*, *39*(2), 217–231.

Crawford, D. (1999), Adaptive mesh refinement in CTH, paper presented at 15th US Army Symposium on Solid Mechanics, U.S. Army, Myrtle Beach, S. C., 12–14 April.

Dey, T., and P. Halleck (1981), Some aspects of size-effect in rock failure, *Geophys. Res. Lett.*, *8*(7), 691–694.

Edgett, K. S., and M. C. Malin (2002), Martian sedimentary rock stratigraphy: Outcrops and interbedded craters of northwest Sinus Meridiani and southwest Arabia Terra, *Geophys. Res. Lett.*, *29*(24), 2179, doi:10.1029/2002GL016515.

Evans, B., and K. L. Kohlstedt (1995), Rheology of rocks, in *Rock Physics and Phase Relations: A Handbook of Physical Constants*, *AGU Ref. Shelf*, vol. 3, edited by T. J. Ahrens, pp. 148–165, AGU, Washington D. C.

Gault, D. E., W. L. Quaide, V. R. Oberbeck, and H. J. Moore (1966), Luna 9 photographs: Evidence for a fragmental surface layer, *Science*, *153*, 985–988.

Goetze, C. (1978), The mechanism of creep in olivine, *Philos. Trans. R. Soc. London, Ser. A*, *288*, 59–119.

Grady, D. E., and R. E. Hollenbach (1979), Dynamic fracture strength of rock, *Geophys. Res. Lett.*, *6*, 73–76.

Grady, D. E., and M. E. Kipp (1980), Continuum modelling of explosive fracture in oil shale, *Int. J. Rock Mech. Min. Sci. Geomech. Abstr.*, *17*, 147–157.

Grady, D. E., and L. Lipkin (1980), Criteria for impulsive rock fracture, *Geophys. Res. Lett.*, *7*, 255–258.

Griffith, A. A. (1920), The phenomena of rupture and flow in solids, *Philos. Trans. R. Soc. London, Ser. A*, *34*, 137–154.

Gromov, V. (1998), Physical and mechanical properties of lunar and planetary soils, *Earth Moon Planets*, *80*, 51–72.

Head, J. N., H. J. Melosh, and B. A. Ivanov (2002), Martian meteorite launch: High-speed ejecta from small craters, *Science*, *298*, 1752–1756.

Herrmann, W. (1969), Constitutive equation for the dynamic compaction of ductile porous materials, *J. Appl. Phys.*, *40*(6), 2490–2499.

Hertel, E. S., Jr., and G. Kerley (1998), *CTH Reference Manual: The Equation of State Package*, *Rep. SAND98–0947*, Sandia Natl. Lab., Albuquerque, N. M.

Holsapple, K. A. (1993), The scaling of impact processes in planetary sciences, *Annu. Rev. Earth Planet. Sci.*, *21*, 333–373.

Holsapple, K. A., and K. R. Housen (2004), The cratering database: Making code jockeys honest, *Lunar Planet. Sci.*, *XXXV*, Abstract 1779.

Holsapple, K. A., and K. R. Housen (2007), A crater and its ejecta: An interpretation of deep impact, *Icarus*, *187*(1), 345–356.

Holsapple, K. A., and R. M. Schmidt (1987), Point source solutions and coupling parameters in cratering mechanics, *J. Geophys. Res.*, *92*(B7), 6350–6376.

Housen, K. R., and K. A. Holsapple (1990), On the fragmentation of asteroids and planetary satellites, *Icarus*, *84*, 226–253.

Housen, K. R., and K. A. Holsapple (1999), Scale effects in strength-dominated collisions of rocky asteroids, *Icarus*, *142*, 21–23.

Ivanov, B. A., and N. A. Artemieva (2002), Numerical modeling of the formation of large impact craters, in *Catastrophic Events and Mass Extinctions: Impact and Beyond*, *Spec. Pap. Geol. Soc. Am.*, *356*, 619–630.

Ivanov, B. A., and A. Deutsch (1999), Sudbury impact event: Cratering mechanics and thermal history, in *Large Meteorite Impacts and Planetary Evolution II*, edited by B. Dessler and R. A. F. Grieve, *Spec. Pap. Geol. Soc. Am.*, *339*, 389–397.

Ivanov, B. A., and V. N. Kostuchenko (1997), Block oscillation model for impact crater collapse, *Lunar Planet. Sci.*, *XXVIII*, Abstract 1655.

Ivanov, B. A., D. Deniem, and G. Neukum (1997), Implementation of dynamic strength models into 2D hydrocodes: Applications for atmospheric breakup and impact cratering, *Int. J. Impact Eng.*, *20*, 411–430.

Jaeger, J. C., and N. G. W. Cook (1976), *Fundamentals of Rock Mechanics*, Chapman and Hall, London.
Kerley, G. (1999), *Equations of State for Composite Materials*, *Rep. KPS99–4*, 52 pp., Kerley Publ., Albuquerque, N. M.
Kerley, G. (2002), *The Effects of Soil Type on Numerical Simulations of Buried Mine Explosions*, *Rep. KTS02–3*, 28 pp., Kerley Publ., Albuquerque, N. M.
Lindstrom, M., V. Shuvalov, and B. Ivanov (2005), Lockne Crater as a result of marine-target oblique impact, *Planet. Space Sci.*, *53*, 803–815.
Lockner, D. A. (1993), Room temperature creep in saturated granite, *J. Geophys. Res.*, *98*, 475–487.
Lockner, D. A. (1995), Rock failure, in *Rock Physics and Phase Relations: A Handbook of Physical Constants*, *AGU Ref. Shelf*, vol. 3, edited by T. Ahrens, pp. 148–165, AGU, Washington, D. C.
Lundborg, N. (1968), Strength of rock-like materials, *Int. J. Rock Mech. Min. Sci. Geomech. Abstr.*, *5*, 427–454.
Malin, M. C., and K. S. Edgett (2000), Sedimentary rocks of early Mars, *Science*, *290*, 1927–1937.
McGlaun, J. M., S. L. Thompson, and M. G. Elrick (1990), CTH: A three-dimensional shock wave physics code, *J. Impact Eng.*, *10*, 351–360.
Melosh, H. J., and B. A. Ivanov (1999), Impact crater collapse, *Annu. Rev. Earth Planet. Sci.*, *27*, 385–415.
Melosh, J. (1989), *Impact Cratering: A Geologic Process*, Oxford Univ. Press, New York.
Mitchell, J. K., L. G. Browell, and W. D. Carrier III (1972), Soil mechanical properties at the Apollo 14 site, *J. Geophys. Res.*, *77*, 5641–5664.
Myers, M. A. (1994), *Dynamic Behavior of Materials*, 688 pp., John Wiley, New York.
Nolan, M. C., E. Asphaug, H. J. Melosh, and R. Greenberg (1996), Impact craters on asteroids: Does gravity or strength control their size?, *Icarus*, *124*, 359–371.
Oberbeck, V. R., and W. L. Quaide (1967), Estimated thickness of a fragmental surface layer of Oceanus Procellarum, *J. Geophys. Res.*, *72*, 4697–4704.
Ohnaka, M. (1995), A shear failure strength law of rock in the brittle-plastic transition regime, *Geophys. Res. Lett.*, *22*(1), 25–28.
Ormö, J., V. V. Shuvalov, and M. Lindström (2002), Numerical modeling for target water depth estimation of marine-target impact craters, *J. Geophys. Res.*, *107*(E12), 5120, doi:10.1029/2002JE001865.
Ormö, J., J. M. Dohm, J. C. Ferris, A. Lepinette, and A. G. Fairén (2004), Marine-target craters on Mars? An assessment study, *Meteorit. Planet. Sci.*, *39*, 333–346.
Paterson, M. S. (1978), *Experimental Rock Deformation—The Brittle Field*, 254 pp., Springer, Berlin.
Piekutowski, A. J. (1977), Cratering mechanisms observed in laboratory-scale high-explosive experiments, in *Impact and Explosion Cratering*, edited by D. J. Roddy et al., pp. 67–102, Pergamon, New York.
Pierazzo, E., A. M. Vickery, and H. J. Melosh (1997), A re-evaluation of impact melt production, *Icarus*, *127*, 408–423.
Pierazzo, E., N. A. Artemieva, and B. A. Ivanov (2005), Starting conditions for hydrothermal systems underneath Martian craters: Hydrocode modeling, in *Large Meteorite Impacts*, edited by T. Kenkmann, F. Horz, and A. Deutsch, *Spec. Pap. Geol. Soc. Am.*, *384*, 443–457.
Poirier, J. (2000), *Introduction to the Physics of the Earth's Interior*, 2nd ed., 312 pp., Cambridge Univ. Press, Cambridge, U.K.
Pratt, H. R., A. D. Black, W. S. Brown, and W. F. Brace (1972), The effect of specimen size on the mechanical properties of unjointed diorite, *Int. J. Rock Mech. Min. Sci.*, *9*, 512–529.
Quaide, W. L., and V. R. Oberbeck (1968), Thickness determinations of the lunar surface layer from lunar impact craters, *J. Geophys. Res.*, *73*, 5247–5270.
Rinehart, J. S. (1968), Intense destructive stresses resulting from stress wave interactions, in *Shock Metamorphism of Natural Materials*, edited by B. M. French and N. M. Short, pp. 31–42, Mono, Baltimore, Md.
Schenk, P. M. (2002), Thickness constraints on the icy shells of the Galilean satellites from a comparison of crater shapes, *Nature*, *417*, 419–421.
Schmidt, R. M., and K. R. Housen (1987), Some recent advances in the scaling of impact and explosion cratering, *Int. J. Impact Eng.*, *5*, 543–560.
Schultz, P. H. (1992), Atmospheric effects on ejecta emplacement, *J. Geophys. Res.*, *97*(E7), 11,623–11,662.
Schultz, R. A. (1995), Limits on strength and deformation properties of jointed basaltic rock masses, *Rock Mech. Rock Eng.*, *28*(1), 1–15.
Shimada, M. (1993), Lithosphere strength inferred from fracture strength of rocks at high confining pressures and temperatures, *Tectonophysics*, *217*, 55–64.
Showman, A. P., and R. Malhotra (1999), The Galilean satellites, *Science*, *286*, 77–84.
Shuvalov, V., H. Dypvik, and F. Tsikalas (2002), Numerical simulations of the Mjølnir marine impact crater, *J. Geophys. Res.*, *107*(E7), 5047, doi:10.1029/2001JE001698.
Shuvalov, V. V., and I. A. Trubestkaya (2002), Numerical modeling of marine target impacts, *Sol. Syst. Res.*, *36*(5), 417–430.
Singh, M. M., and P. J. Huck (1973), Large scale triaxial tests on rocks, in *New Horizons in Rock Mechanics: Proceedings of the 14th Symposium on Rock Mechanics*, pp. 35–60, Am. Soc. Civ. Eng., Reston, Va.
Wilcox, B. B., M. S. Robinson, P. C. Thomas, and B. R. Hawke (2005), Constraints on the depth and variability of the lunar regolith, *Meteorit. Planet. Sci.*, *40*(5), 695–710.
Wunnemann, K., and B. A. Ivanov (2003), Numerical modeling of the impact crater depth-diameter dependence in an acoustically fluidized target, *Planet. Space Sci.*, *51*, 831–845.
Wunnemann, K., G. S. Collins, and H. J. Melosh (2006), A strain-based porosity model for use in hydrocode simulations of impacts and implications for transient crater growth in porous targets, *Icarus*, *180*(2), 514–527.
Zhang, L. (2005), *Engineering Properties of Rocks*, 304 pp., Elsevier, Amsterdam.

L. E. Senft and S. T. Stewart, Department of Earth and Planetary Sciences, Harvard University, 20 Oxford Street, Cambridge, MA 02138, USA. (lsenft@fas.harvard.edu; sstewart@eps.harvard.edu)